Using electron backscatter diffraction to measure full crystallographic orientation in Antarctic land-fast sea ice

PAT WONGPAN,[1] DAVID J. PRIOR,[2] PATRICIA J. LANGHORNE,[1] KATHERINE LILLY,[2] INGA J. SMITH[1]

[1]*Department of Physics, University of Otago, 730 Cumberland Street, Dunedin 9016, New Zealand*
[2]*Department of Geology, University of Otago, 360 Leith Street, Dunedin 9016, New Zealand*
Correspondence: Pat Wongpan <pat.wongpan@postgrad.otago.ac.nz>

ABSTRACT. We have mapped the full crystallographic orientation of sea ice using electron backscatter diffraction (EBSD). This is the first time EBSD has been used to study sea ice. Platelet ice is a feature of sea ice near ice shelves. Ice crystals accumulate as an unconsolidated sub-ice platelet layer beneath the columnar ice (CI), where they are subsumed by the advancing sea–ice interface to form incorporated platelet ice (PI). As is well known, in CI the crystal preferred orientation comprises dominantly horizontal *c*-axes, while PI has *c*-axes varying between horizontal and vertical. For the first time, this study shows the *a*-axes of CI and PI are not random. Misorientation analysis has been used to illuminate the possible drivers of these alignments. In CI the misorientation angle distribution from random pairs and neighbour pairs of grains are indistinguishable, indicating the distributions are a consequence of crystal preferred orientation. Geometric selection during growth will develop the *a*-axis alignment in CI if ice growth in water is fastest parallel to the *a*-axis, as has previously been hypothesised. In contrast, in PI random-pair and neighbour-pair misorientation distributions are significantly different, suggesting mechanical rotation of crystals at grain boundaries as the most likely explanation.

KEYWORDS: crystal growth, glaciological instruments and methods, ice crystal studies, sea ice–ice shelf interactions

1. INTRODUCTION

Ice crystals in nature have hexagonal symmetry (ice Ih; Pauling, 1935), with three *a*-axes (one a linear combination of the other two) lying in the basal plane and a *c*-axis pointing perpendicular to this plane (e.g., Weeks, 2010; Petrich and Eicken, 2017). Due to the kinetics of growth, ice grows up to ∼100 times faster in the basal plane compared with the thickening in the *c*-axis direction (Hillig, 1959).

The initial skim of sea ice grows by vertical heat conduction from the ocean to the atmosphere. This initial layer of sea ice is composed of crystals with random orientations, usually because of turbulence in the water (Weeks, 2010). Crystals with *c*-axis close to the horizontal grow faster so that other orientations are eliminated. This geometric selection (Kolmogorov, 1976) results in a column-like structure called columnar ice (CI) with vertically elongated grains, each with a horizontal *c*-axis. Sea ice that grows by heat conducted to the atmosphere is called congelation ice. The most common form of congelation ice has a columnar structure.

When sea water freezes, salt is rejected at the ice/water interface. The transport of salt into the bulk liquid occurs at a slower rate than the transport of heat, causing the brine immediately ahead of the interface to be constitutionally supercooled (e.g., Weeks, 2010). Driven by the growth kinetics of ice and by the need to transport salt from the freezing face, the interface develops a morphological instability (e.g., Weeks, 2010; Petrich and Eicken, 2017). The interface evolves into the lamellar structure shown in Fig. 1a. Lamellae (also called cells or platelets in the sea ice literature) within individual columnar grains, protrude into the underlying sea water (Fig. 1a). As the ice/water interface advances (grows) liquid brine is trapped between lamellae creating a lamellar structure of ice layers and brine inclusions within a single columnar grain. Lamellae lie parallel to the basal plane within each columnar grain. Bennington (1963) pointed out that exchange of salt-rich brine at the interface is not inhibited where columnar grains have horizontal *c*-axes and lamellae are oriented vertically. In contrast, grains where the *c*-axis is at a high angle to the horizontal may form a trap for impurities. This means that the salinity, and hence the temperature, at the growing surface of a grain is dependent on its orientation.

About 44% of the Antarctic coastline is occupied by ice shelves, massive glacial bodies that have extended offshore to float on the ocean (Drewry and others, 1982). As illustrated in Fig. 1b, land-fast sea ice near an ice shelf may be influenced by the outflow of supercooled water (water colder than its freezing point) from under the ice shelf (Foldvik and Kvinge, 1974; Lewis and Perkin, 1986). We use the term *frazil* for tiny (millimetre dimensions) crystals in the water column and *platelet* for these crystals when they are in contact with the sea ice cover. Frazil in the supercooled outflow may accumulate under the sea-ice cover to form a porous, friable sub-ice platelet layer (Langhorne and others, 2015, and references therein). The sub-ice platelet layer hosts the highest concentration of sea-ice algae in the biosphere (Arrigo and others, 2010). With low variability in temperature and salinity, plenty of space and unlimited nutrients supplied by fluid flow, this highly porous sub-ice platelet layer is the main reason for the difference of the biomass accumulation between the Arctic and Antarctica (Arrigo, 2017).

The advancing interface of congelation ice freezes the interstices in the sub-ice platelet layer, consolidating it to
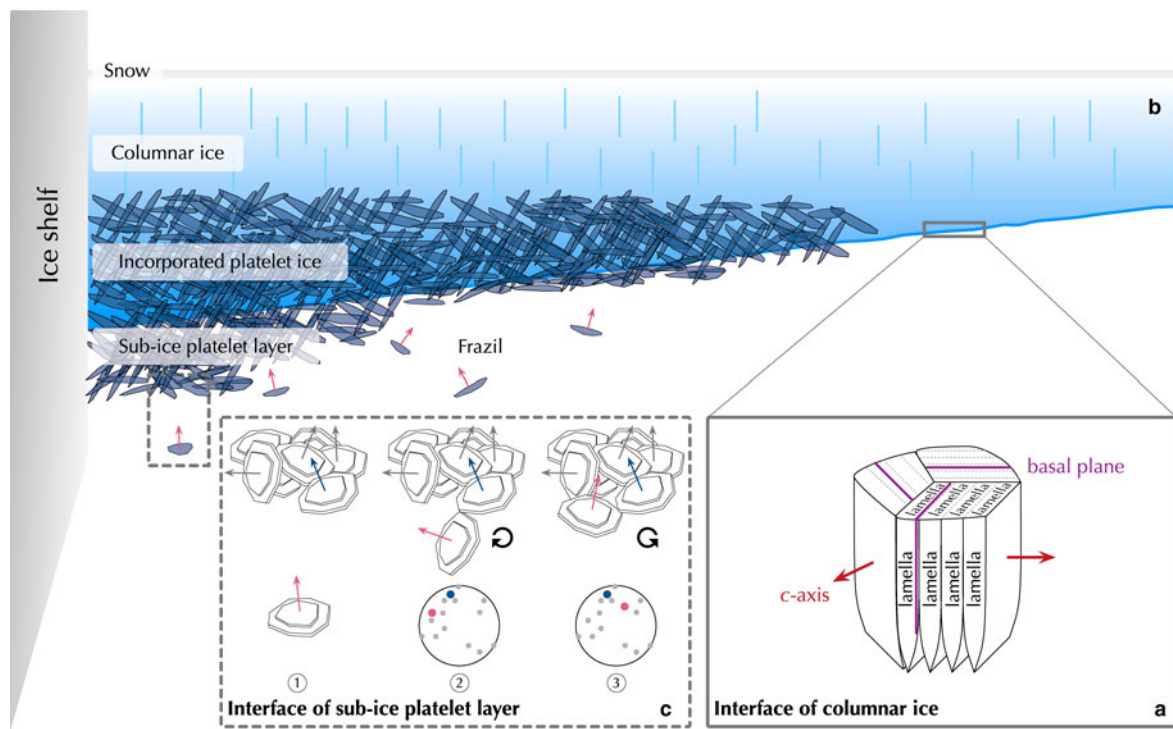
Fig. 1. (a) Three columnar ice grains with lamellar internal structure related to the growth of the ice/water interface. Magenta lines are traces of the basal plane. (b) Schematic of sea-ice formation with distance from an ice shelf, showing columnar ice, incorporated platelet ice and a sub-ice platelet layer. (c) Sub-ice platelet layer dynamics in which frazil arrives under the ice cover (c.1), the platelet crystal rotates (c.2) and again (c.3) to achieve mechanical stability. Stereonets (described in Fig. 5) are also shown in c.2 and c.3 to represent the process. Arrows (on platelet crystals) and dots (on stereonets) represent c-axes.

form incorporated platelet ice (PI). This process has been observed in thick section analysis (Gow and others, 1982; Jeffries and others, 1993; Smith and others, 2001) and simulated by sub-ice platelet layer dynamics (Dempsey and others, 2010; Wongpan and others, 2015) as illustrated in Fig. 1c. In these simulations a flux of frazil crystals arrived at the ice/water interface and each crystal was permitted to rotate in all three degrees of freedom until it was mechanically stable. A sub-ice platelet layer was predicted to form if the flux of frazil crystals exceeded the rate of advance of the congelation interface (Dempsey and others, 2010). If the rate of advance of congelation ice is faster then individual frazil crystals may be incorporated into CI but no sub-ice platelet layer will form.

The structural evolution of PI has been interpreted based on c-axis orientation alone (e.g., Gow and others, 1982; Gough and others, 2012a; Dempsey and Langhorne, 2012) because optical measurement using the universal stage (Langway, 1958) can only measure the c-axis. In other words, an ice crystal was assumed to have cylindrical symmetry, instead of hexagonal symmetry (e.g., Morawiec, 1995). Due to this limitation, grain boundaries in sea ice are usually constructed based on the difference of c-axis orientation among neighbour grains and the description of rotation around the c-axis is impossible.

One of the challenges is to measure full crystallographic orientation for sea ice (Weeks, 2010). The full orientation was used to quantify microstructural processes at grain boundaries in petrology (e.g. Wheeler and others, 2001). Misorientation distributions can be used to indicate whether physical interaction has occurred between grains, or whether the misorientations are just a consequence of the sample crystallographic preferred orientation (CPO)

(Wheeler and others, 2001). To get a-axis orientations in sea ice, observations of etch pits have been used (Kawamura and Ono, 1980; Matsuda and Wakahama, 1978; Matsuda, 1979) but this is technically challenging and time-consuming. The only study of a-axes in sea ice is that of Kawamura and Ono (1980) on young Arctic sea ice (< 0.22 m thick). For this very thin sea ice, they did not find strong preferred orientation of a-axes, but the ice was also too thin to display the typical CPO of c-axes in the horizontal plane. The Laue X-ray diffraction method has been used to make full orientation measurements of ice crystals in ice-sheet samples from Greenland (Miyamoto and others, 2005, 2011) but has not been applied to sea-ice samples to our knowledge. Electron backscatter diffraction (EBSD) is a scanning electron microscope (SEM) method that enables the full crystal orientation of specific points in a sample to be measured (Prior and others, 1999). The technology to carry out EBSD on the ice was developed in the mid 2000s (Iliescu and others, 2004; Obbard and others, 2006; Piazolo and others, 2008). Prior and others (2015) made the technique more routine and developed methods to work on large ice samples, enabling the technique to be useful to the large crystals found in the sea-ice studies. In this paper, we present a pilot study of sea-ice microstructures based on full crystal measurements made by EBSD. We present and interpret EBSD data collected from samples from across the transition from columnar ice to incorporated platelet ice.

2. SAMPLES AND METHODS

2.1. Study sites

The sea-ice core analysed in this paper was retrieved in November 2011 from McMurdo Sound, Antarctica (Fig. 2a)
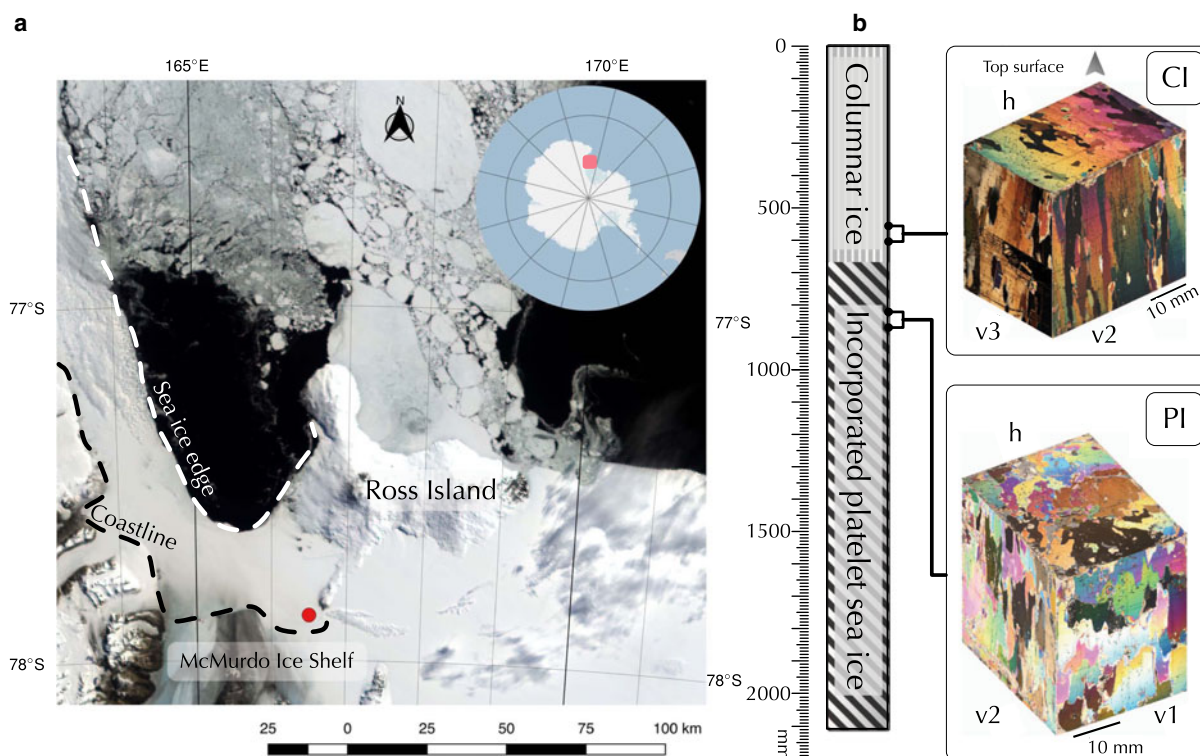
Fig. 2. (a) Location of the study site in eastern McMurdo Sound in 2011 where the ice core was taken. The satellite image was taken on 29 November 2011 by MODIS Terra (https://lance-modis.eosdis.nasa.gov) and overlaid on Quantarctica v2.0, a free GIS package for Antarctica (http://quantarctica.npolar.no/). (b) Core sketch based on Hughes and others (2014) and thin sections of samples of interest.

from the east site of Hughes and others (2014). This ice core was transferred from the sea-ice site to the transitional facility at the University of Otago and was kept in storage at − 30 °C. The physical and oceanographic conditions associated with this ice core were described by Hughes and others (2014). The core length was 2.11 m and the columnar-incorporated platelet ice transition (Fig. 2b) was reported to be at 0.67 m (Hughes and others, 2014). We selected samples to be above (CI) and below (PI) this transition. CI was from 0.55 to 0.60 m and PI was from 0.82 to 0.87 m (Fig. 2b).

2.2. Sample preparation and EBSD data collection

We followed the protocol of Prior and others (2015) to perform EBSD on sea ice. First, samples were prepared in a cold room facility at − 25 °C. We cut samples from a half cylinder into a cube (Figs. 3a, b). From the cube, we sliced

three surfaces and named them as CI-h and PI-h (horizontal cross sections) and CI-v2, CI-v3, PI-v1 and PI-v2 (vertical cross sections, Figs. 3c and 2b). We mounted samples onto copper plates. To obtain flat surfaces, samples were microtomed then ground using fine to ultra-fine sandpapers in the cold room. Samples were then cooled slowly to reach liquid nitrogen temperature and moved from the cold room to the SEM laboratory in a dry shipper at liquid nitrogen temperature. Salt was expelled at grain boundaries during cold room preparation. This salt covered the sample surface (Fig. 4a). To achieve a smooth surface for EBSD and single phase EBSD scanning, cold grinding (below − 60 °C) of the surface was conducted in the SEM laboratory to remove the solid salt. Samples were transferred into the SEM chamber through a nitrogen-filled glove box to reduce frost. Surface sublimation in the SEM chamber, by pressure cycling (Prior and others, 2015), removed frost and surface
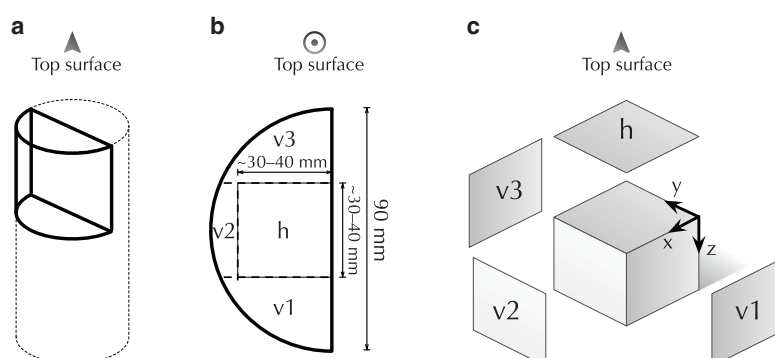

Fig. 3. (a) The ice core was cut in half. (b) The top view shows the half cylinder was cut into four surfaces. (c) The side view of the cut and four surfaces.
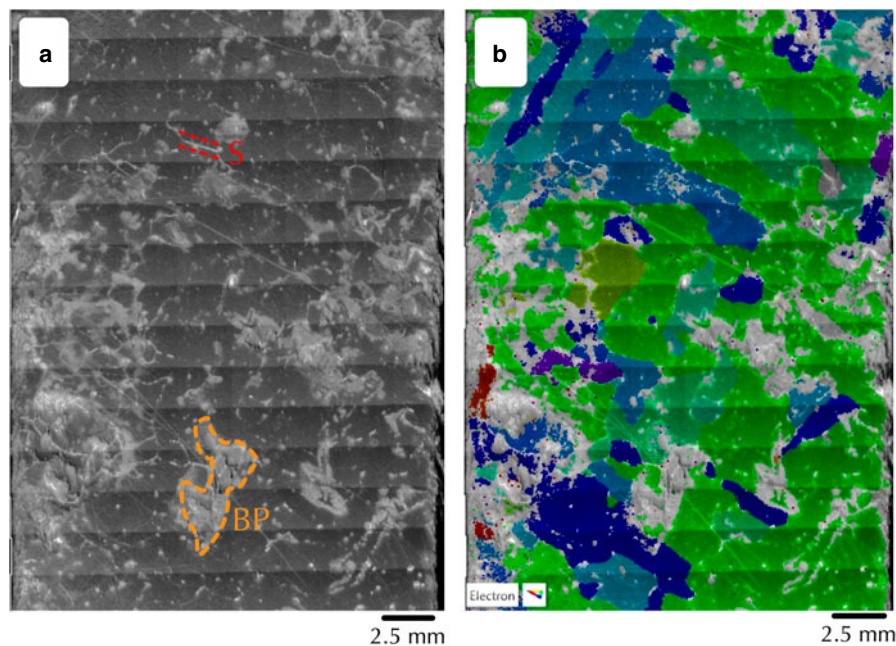
Fig. 4. Some issues for EBSD on sea ice. (a) Secondary electron image montage of CI-h from the SEM shows salt (bright flecks on grain boundaries: S) which was expelled along grain boundaries and exposed brine pockets (grey holes: BP). (b) Image to show level of indexing in raw EBSD data. Coloured pixels have a good quality EBSD solution. Non-indexed pixels are transparent so that the underlying greyscale image (as in Fig. 4a) is visible.

damage. EBSD data were collected on a Zeiss SIGMAVP FEGSEM using 30 kV accelerating voltage and ~100 nA beam current. 5 Pa to 20 Pa of nitrogen gas pressure was used to control charging and sample stage temperatures were kept colder than − 80 °C. EBSD patterns were imaged with a Nordlys F camera and raw data acquired using the AZTEC software from Oxford Instruments. Data were processed and imaged using custom-written MATLAB code calling appropriate algorithms from the MTEX toolbox (Bachmann and others, 2010).

The data quality of EBSD on natural sea ice had some limitations. First, brine and air pockets were an impediment to obtaining flat surfaces during sample preparation (Fig. 4a). Analysis points in brine pockets give no diffraction pattern and are 'non-indexed' pixels in the EBSD data (Fig. 4b). Non-indexed pixels, sometimes in patches, also occur where the sample comprises biological matter or nonalgal particulates and where there is surface contamination or poor sample polish. The versatile grain reconstruction algorithm by Bachmann and others (2011) was used to enable grains to be reconstructed without artefacts due to the non-indexed pixels.

2.3. Full orientation and colatitude analysis

EBSD yields full orientations at each pixel. There are various ways to present full orientations (e.g., Randle, 1992; Randle and Engler, 2009) and understanding some of these representations can be challenging. We will present each orientation in separate stereonets (Fig. 5) for the c-axes $\langle 0001 \rangle$, the a-axes $\langle 11\bar{2}0 \rangle$ and the poles to m-planes $\{10\bar{1}0\}$. Each measured orientation (Fig. 5a) gives rise to one c-axis, three a-axes and three m-planes (Figs. 5b-d). A parameter that is frequently used in the analysis of ice CPOs (e.g., Treverrow and others, 2010) and is derived from the c-axis orientation is the colatitude. The colatitude (γ) of a grain is the angle

between c-axis of that grain and the vertical (z) direction (Fig. 5). The maximum colatitude is $\gamma = 90°$. This colatitude can be used to distinguish between columnar and platelet ice crystals. Columnar ice crystals are horizontal ($\gamma \approx 90°$) while those of platelet crystals are varied and include vertical orientations ($\gamma \approx 0°$) (Jeffries and others, 1993). Treverrow and others (2010) used colatitude distributions to analyse marine ice formation, an analogous ice type to PI found beneath ice shelves. We decomposed grains for each sample into three subsets based on their colatitudes: sub-vertical grains ($\gamma < 30°$), inclined grains ($30° \leq \gamma \leq 60°$) and sub-horizontal grains ($\gamma > 60°$).

2.4. Misorientation analysis

The misorientation is the rotation needed to map one orientation onto another (see Wheeler and others (2001), their
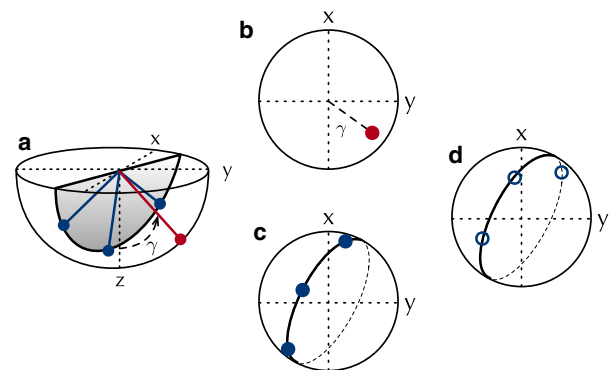

Fig. 5. (a) A three-dimensional representation shows the c-axis (red stem), the basal plane (gray plane) and three a-axes (three blue stems) and has the colatitude γ measured from z to the c-axis. Three separate stereonets show the projection of the respective unit vectors onto the X–Y plane (b) c-axis (red dot), (c) a-axes (three blue closed dots) and (d) m-planes (three blue open dots).
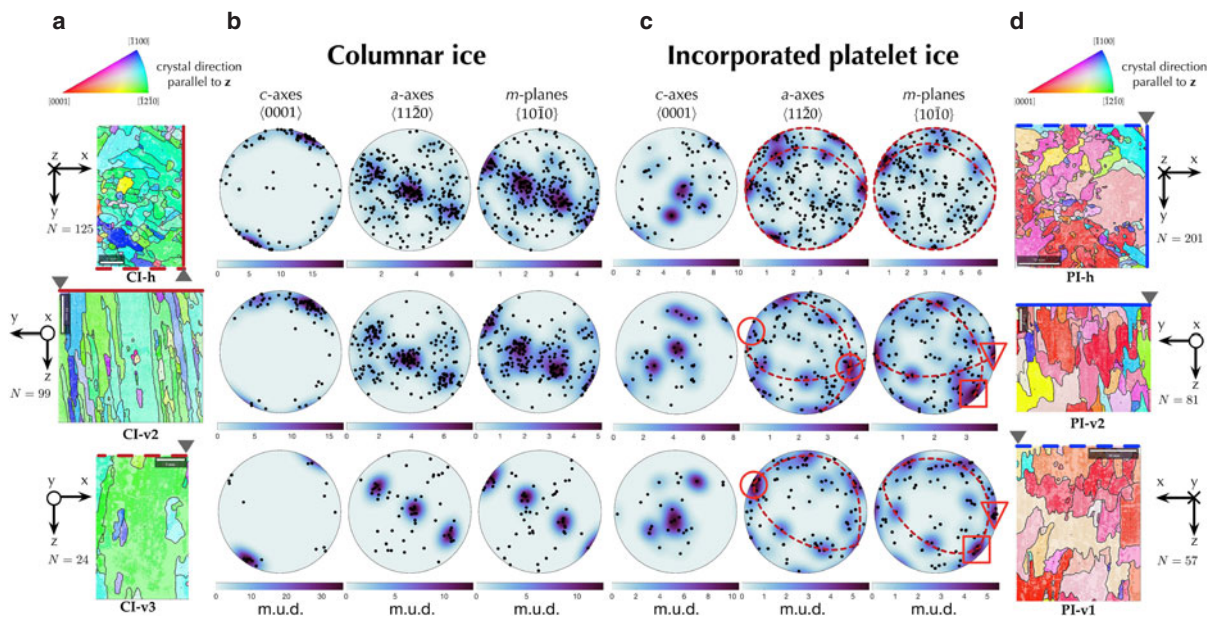
Fig. 6. EBSD maps from columnar ice samples (a) and incorporated platelet ice samples (d) and corresponding CPOs presented as stereonets (b and c). The CPOs are all plotted in the same reference frame as shown in Fig. 5 (z in the centre of the net). (a and d) EBSD map with 1 μm step size coloured according to the inverse pole figure shown on top and overlaid by grain construction from MTEX based on 5° misorientation angle threshold. Note that the grey triangles mark the common corner of the three sections. Solid and dashed lines denote the shared edges. (b and c) Orientations for each grain (black dots) are overlaid by contours calculated from the dataset orientation distribution function. Contours are multiples of uniform distribution (m.u.d.). Stereonets are plotted on equal area, lower-hemisphere projections (see Fig. 5). All pixels in (a and d) are used for contours, so that contours are weighted by grain area in the maps. Red dashed lines, circles, squares and triangles are visual aids for weak alignments of a-axes and m-planes in incorporated platelet ice interpreted in the text.

Fig. 1a). The most common way to represent misorientation is as an axis of rotation (misorientation axis) and an angle of rotation (misorientation angle). In ice, because of the hexagonal symmetry, there are 12 different angle axis pairs that describe the misorientation equally well (see Wheeler and others (2001), their Fig. 1b). By convention, we choose the pair with the minimum misorientation angle (Wheeler and others, 2001). Two types of misorientation distribution can be calculated from EBSD data (Wheeler and others, 2001). The random-pair and the neighbour-pair misorientation distributions are constructed by selecting pairs of grains at random, or selecting neighbouring grains, respectively. These distributions are visualised using histograms. Both histograms will differ from the curve for a random set of orientations if there is a CPO. Differences between the random and neighbour pair distributions imply that there is a physical interaction between grains (Wheeler and others, 2001). We excluded misorientation angles <5° from the statistical analysis because small misorientations data are prone to errors (Prior, 1999). Note that the maximum misorientation angle for hexagonal symmetry is 93.8° (Morawiec, 1995).

3. RESULTS

3.1. Sea-ice structure overview and grain properties

An overview of microstructures and CPOs for all samples are plotted in Fig. 6. Individual grains were segmented using the algorithm of Bachmann and others (2011) with a threshold of 5° as the lowest misorientation for a grain boundary. The statistics of grains for each sample are listed in Table 1. Data from CI-h and PI-h (top rows in Figs. 6b, c) are segmented to distinguish different colatitudes in Fig. 7.

Columnar ice average grain area, perimeter and aspect ratio (Table 1) of the horizontal cross section (CI-h) are two to three times smaller than those of vertical samples (CI-v2, CI-v3). In particular, the mean grain aspect ratio of CI is about two for the horizontal cross section but increases to between two and four for vertical sections. This reflects the column-shaped grains aligned vertically. CI-v3 shows the smallest (24) number of grains compared with other samples because it is dominated by the one big columnar grain (Fig. 6a). The contouring stereonets (Fig. 6b) show three clusters of a-axes lying at 60° to each other, within a plane perpendicular to the c-axis cluster. One a-axis cluster is vertical. Three clusters of poles to m-planes also lie in the plane perpendicular to the c-axis cluster, each lying half way between two a-axis clusters. These patterns are shown in all three sample orientations (CI-h, CI-v2 and CI-v3) and show that the CPO approximates a single crystal with a sub-horizontal c-axis and a vertical a-axis. For colatitudes (Fig. 7) most of c-axes (119 out of 125 grains) are sub-horizontal.

Table 1. Grain properties

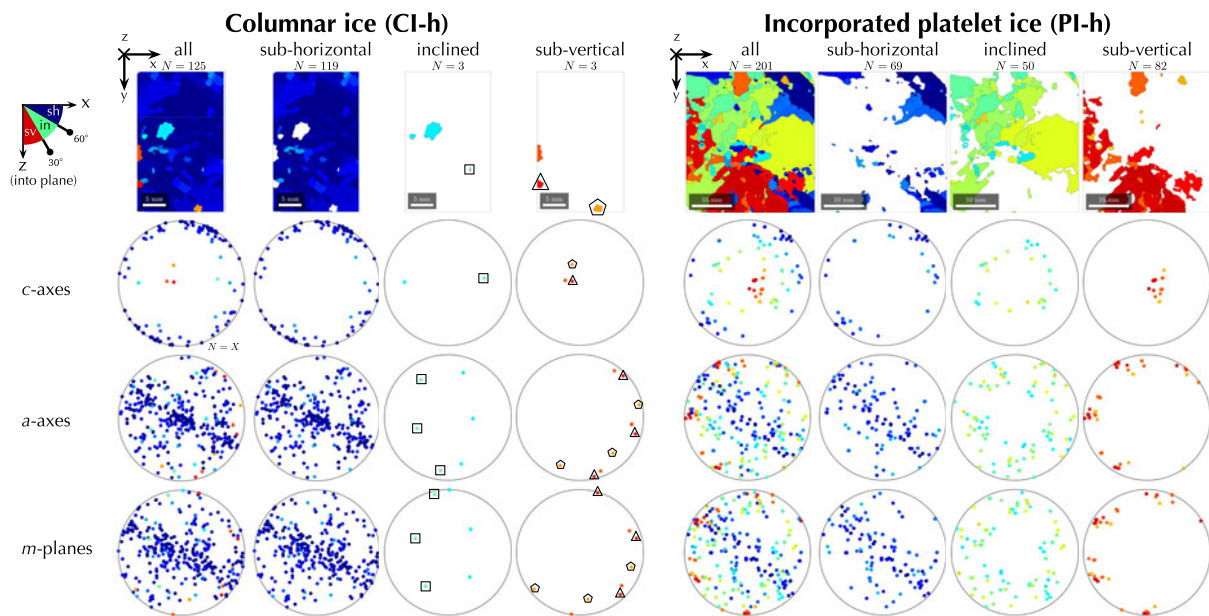| Sample	Columnar ice			Incorporated platelet ice		
	CI-h	CI-v2	CI-v3	PI-h	PI-v2	PI-v1
Sample size (mm²)	576.9	1363.2	415.1	1112.4	701.6	883.7
Number of grains	125	99	24	201	81	57
Mean area (mm²)	4.6	13.8	17.4	5.5	8.7	15.5
Mean perimeter (mm)	8.7	18.9	13.6	8.6	13.3	18.1
Mean aspect ratio	1.8	3.8	2.7	1.8	2.3	2.0

Fig. 7. First column from top to bottom row: EBSD map of all grains of CI-h and PI-h coloured based on their colatitudes and the corresponding stereonets for each plane. Second, third and fourth columns show subsets for sub-horizontal (sh), inclined (in) and sub-vertical grains (sv). Note that one *c*-axis orientation has three corresponding *a*-axes and *m*-planes (Fig. 5).

In contrast to CI, for PI the differences between grain sizes and the aspect ratios of horizontal and vertical thin sections are small (Table 1). Furthermore the mean grain aspect ratio of incorporated platelet ice remains approximately two for both horizontal and vertical sections. In Fig. 6c the patterns of *a*-axes and poles to *m*-planes are more complex in PI than in CI. In all three section orientations there are at least two planes (red great circles) that contain clusters of *a*-axes and poles to *m*-planes. In section PI-v1 there is a single, sub-horizontal, dominant cluster of the *a*-axes (red circle) and a dominant cluster (red square) and secondary cluster (red triangle) of poles to *m*-planes. In section PI-v2 there is a single dominant *a*-axis cluster (red circle) that overlaps the orientation of the dominant cluster in PI-v1. Two dominant clusters of poles to *m*-planes in PI-v2 match the positions of dominant clusters in PI-v1. Section PI-h has dominant clusters of both *a*-axes and poles to *m*-planes slightly oblique to the clusters in the vertical sections. The data from the vertical sections suggest on the scale of the sample there is a preferred orientation of *a*-axes and of the poles to *m*-planes lying within a sub-horizontal plane. The data from the vertical sections suggest that within the sample size there is a weak preferred orientation of *a*-axes and of the poles to *m*-planes within a sub-horizontal plane. For colatitudes, in PI (PI-h) there are 69 grains in the sub-horizontal group, 82 grains in inclined and 50 grains in sub-vertical (Fig. 7). Grains with similar colatitude angles tend to be physically close to each other, possibly because the ice crystals form clusters as they accumulate and grow at the ice/ocean interface.

3.2. Misorientation and colatitude analyses

Results of misorientation and colatitude analyses are illustrated in Figs. 8 and 9, respectively. The theoretical misorientation and colatitude distributions from Morawiec (1995) and Treverrow and others (2010) for a sample with no CPO are also illustrated. Note that theoretical results of the cylindrical crystal symmetry for misorientation angle (Morawiec,

1995) and colatitude description (Treverrow and others, 2010) are equivalent.

In Fig. 8a the random-pair distribution of misorientation angles of CI deviates from the curve for no CPO, with a peak appearing at low misorientation angle (~5°–35°) and a trough at higher misorientation angle (40°–90°). The random-pair and neighbour-pair distributions have similar characteristics. To test whether these two distributions are significantly different we performed a two-sample Kolmogorov–Smirnov test (K–S test). In Fig. 8c, empirical cumulative distribution functions (ECDF) are plotted to ascertain the similarity between the random-pair and neighbour-pair distributions. P-values from the K–S test are calculated using the maximum difference between the two ECDFs and the number of pairs in each sample. The null hypothesis is that the two distributions are drawn from the same data set. We used the 5% significance level. We reject the null hypothesis if the p-value is <0.05. The test fails to reject the null hypothesis for CI (p-value = 0.1, Fig. 8c) which means the random-pair and neighbour-pair distributions are indistinguishable in our dataset. The colatitude distributions of CI strongly deviated from the random curve (Figs. 7 and 9a). In Fig. 9c the colatitude difference distributions of both neighbour-pair and random-pair are dominated by small (0°–30°) angles and are approximately zero outside this range.

For PI (Fig. 8b) the random-pair distribution of misorientation angle is compared with the curve for no CPO. From the K–S test, the difference between the random-pair and neighbour-pair misorientation distributions is significant in PI (p-value < 0.0001). The colatitude distribution in PI is also closer to the random curve (see Fig. 9b) than CI but has some high peaks at low colatitude (Fig. 9b). Random-pair and neighbour-pair colatitude difference distributions are very similar to each other: this is true in both columnar (Fig. 9c) and platelet ice (Fig. 9d). This indicates that the difference distributions are just a function of the *c*-axis preferred orientations (as represented in stereonets and colatitude distributions).
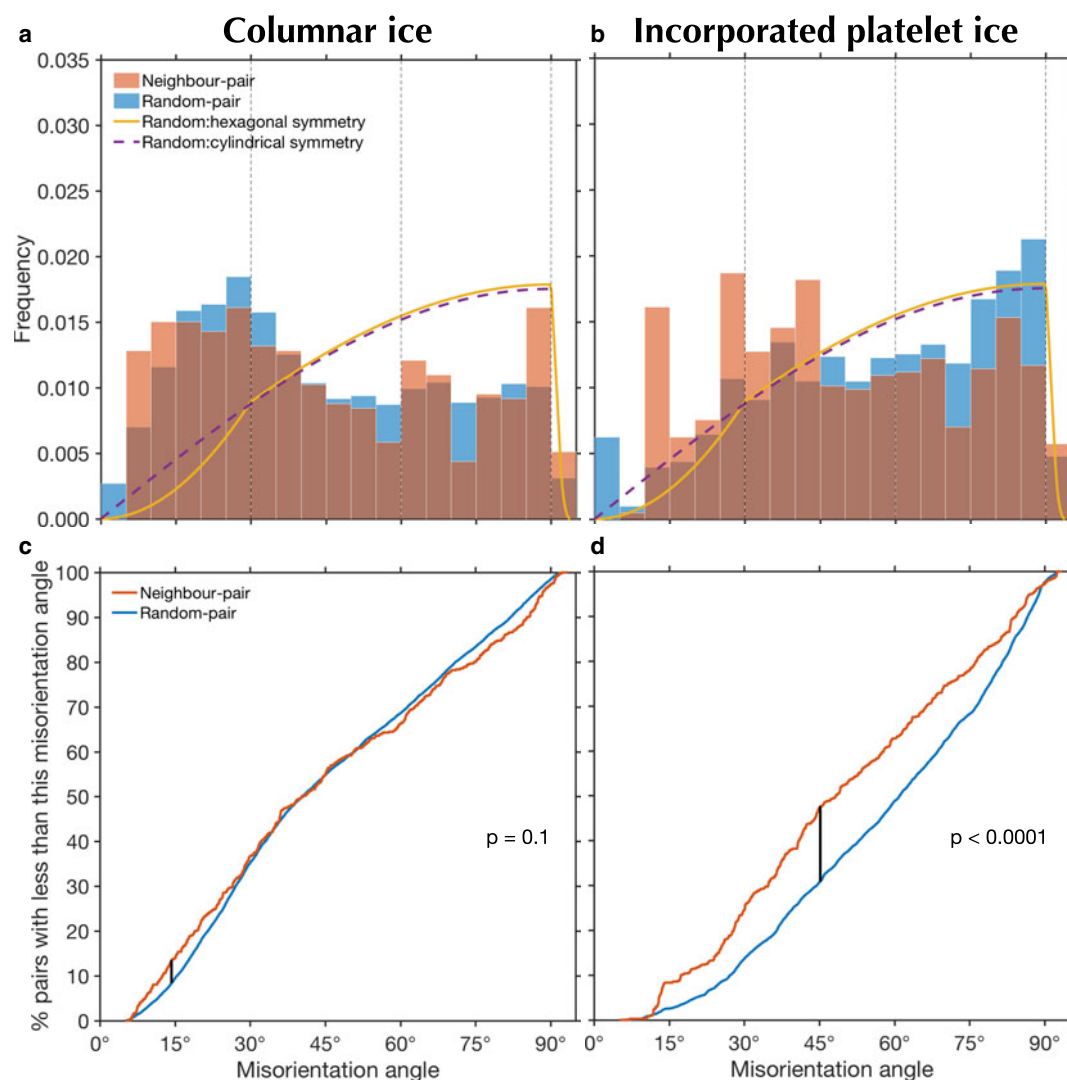
Fig. 8. (a) Neighbour-pair and random-pair misorientation angle distributions of columnar ice (CI-h, CI-v2 and CI-v3 grouped together) and (b) incorporated platelet ice (PI-h, PI-v2 and PI-v1 grouped together). Solid and dashed lines are theoretical distributions of misorientation angles for no CPO for crystals with hexagonal and cylindrical symmetry, respectively (Morawiec, 1995). (c) and (d) are empirical cumulative distribution functions (ECDF) of misorientation angle. Note that p represents the p-value from a two-sample Kolmogorov–Smirnov test.

4. DISCUSSION

In sea ice, it is well known that geometric selection ensures that grains where the c-axis is sub-horizontal grow to form columns. Frazil crystals from ice shelf/ocean interaction arrive and are accreted and grow under the advancing interface of the sea-ice cover as platelet crystals (Figs. 1b and 10a). This suggests that the microstructure of the PI is the blending of crystals from two different physical origins: the CI grains and platelet crystal grains (Figs. 10d, e) while in CI it evolves from a single origin.

In CI the CPO is a horizontal clustering of c-axes and vertical a-axes (Figs. 6a, b). This alignment of c-axes in the horizontal plane in CI is probably explained by the dominant current direction at the time of formation (Langhorne, 1983; Langhorne and Robinson, 1986). The dominance of vertical a-axes in thick columnar sea ice is a new result and is consistent with Weeks (2010)'s hypothesis that growth is fastest in the a-axis direction. There are some low-colatitude crystals in CI-h and CI-v2 which may be platelet crystals (Fig. 10d) that have been incorporated because the frazil flux is much less than the growth rate of columnar ice (Dempsey and others, 2010).

The PI is complex (Figs. 6c, d). Sub-vertical grains are likely to be platelet crystals that float up to the sea ice because most c-axes of CI crystals are sub-horizontal (Fig. 10c). Inclined grains are those that have mechanically rotated beneath the rough ice interface of the sub-ice platelet layer as simulated by Dempsey and others (2010) and Wongpan and others (2015). The crystal orientation data (Figs. 10d, e) illustrate that incorporated platelet ice may be a blending of columnar ice and accumulated frazil. This subset is similar to the majority of marine ice banding accretion (Fig. 11 of Treverrow and others (2010)).

From the K–S test the difference between the random-pair and neighbour-pair misorientation distributions is statistically significant in PI but not in CI (Figs. 10b, c). This implies that in PI, boundary processes may play a role or that more than one domain is present (Wheeler and others, 2001). The mechanical rotation modelled in Dempsey and others (2010) and Wongpan and others (2015) is the most likely process to orient the crystals in the sub-ice platelet layer. The presence of brine in the interstices among platelet crystals suggests that they are relatively free to rotate (Dempsey and others, 2010). These interstices were probably filled with both settling
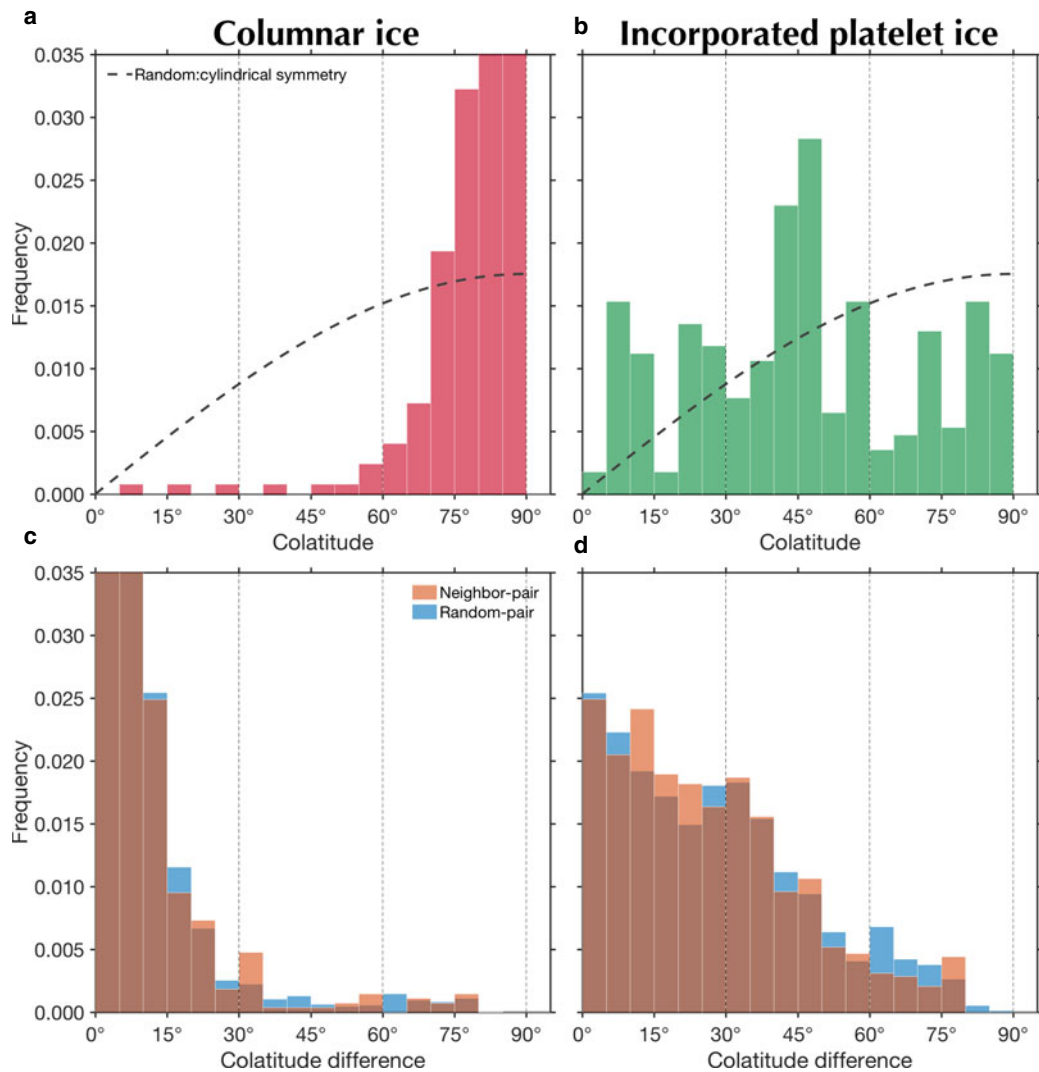
Fig. 9. Colatitude distributions of columnar ice (a) samples (CI-h, CI-v2 and CI-v3e grouped together) and incorporated platelet ice (b) samples (PI-h, PI-v2 and PI-v1 grouped together), respectively. Dashed lines are theoretical distribution of colatitudes for no CPO for crystals with cylindrical symmetry (Morawiec, 1995; Treverrow and others, 2010). Neighbour-pair and random-pair colatitude-difference distributions for columnar (c) and incorporated platelet ice (d).
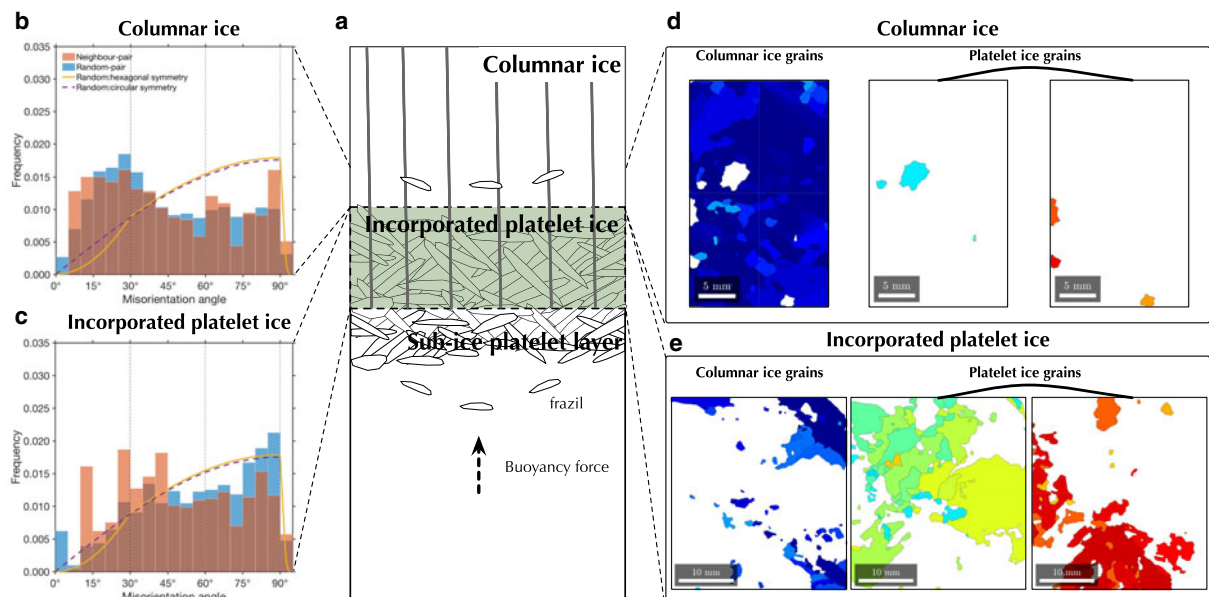

Fig. 10. (a) Schematic illustration of important processes in controlling grain orientations in the formation of incorporated platelet ice. (b) and (c) are misorientation angle distributions from Figs. 8a, b. In (d) and (e) CI and PI grains are tentatively identified according to the colatitude in Fig. 7.

platelet crystal growth and congelation ice as simulated with heat and mass transfer in Wongpan and others (2015). The decrease in porosity during the incorporation process produces the interlocking microstructures of columnar and ice crystals in PI (Fig. 10e) similar to the cumulated olivines in a feldspathic peridotite (Wheeler and others, 2001).

Sea ice is well known for its sub-metre scale spatial inhomogeneities, especially in salinity distribution (Tucker and others, 1984; Eicken and others, 1991; Gough and others, 2012b). However, Weeks and Gow (1980) observed 95% of the alignment of *c*-axes in CI along 1200 km of the Alaska coastline were clusters in the horizontal plane. In CI the physical driver of alignment is the direction of the current which has an influence at the regional scale, and is relatively much larger than the sample size. In PI, on the other hand, the alignment of crystals is mainly driven by the mechanical rotation of individual crystals (Dempsey and others, 2010; Wongpan and others, 2015). The small sample size limits the generalisability of our results.

In future work, the understanding of the link between the mechanical rotation and *a*-axis alignment in PI could be improved by laboratory experiments and image capturing approaches similar to those used to study frazil ice formation (McFarlane and others, 2014, 2015). Recently McFarlane and others (2017) also adapted optical techniques to suit field observations. Visual evidence from both laboratory and the field could be combined with the EBSD technique. Misorientation and colatitude analyses explained in this paper could then be used to investigate the role of rotation on the alignment of *a*-axes in PI.

5. CONCLUSION

For the first time, EBSD has been used for the analysis of sea-ice microstructure and crystallographic preferred orientation in columnar and incorporated platelet ice. The full orientations obtained from EBSD contribute additional information of *a*-axis orientations not available optically. CI with *c*-axes horizontal has *a*-axes vertical. The CPO of *c*-axes in CI can be explained by geometric selection and the influence of ocean current at the time and location of the sea-ice formation, as is well known. Further the CPO of *a*-axes were found to have alignment in the vertical in agreement with the hypothesis of Weeks (2010) that growth is fastest in the *a*-axis direction. On the other hand, PI has *c*-axes between vertical and horizontal and there appears to be a weak alignment of *a*-axes. In PI, misorientation analysis shows the distribution of misorientation angles between any two grains in contact is not predicted by the orientation distribution of grains. This implies that there is mechanical interaction between platelet crystals in contact with each other that controls the boundary misorientation. The small sample size limits the generalisability of our results.

REFERENCES

Arrigo KR (2017) Sea ice as a habitat for primary producers. In Thomas DN ed. *Sea Ice*. John Wiley & Sons Ltd, Hoboken, United States, 352–369 (doi: 10.1002/9781118778371.ch14)

Arrigo KR, Mock T and Lizotte MP (2010) Primary producers and sea ice. In Thomas DN & Dieckmann GS, eds. *Sea Ice*, 2nd edn. Wiley-Blackwell, Oxford, UK, 283–325 ISBN 9781444317145 (doi: 10.1002/9781444317145.ch8)

Bachmann F, Hielscher R and Schaeben H (2010) Texture analysis with MTEX – free and open source software toolbox. *Solid State Phenomena*, **160**, 63–68

Bachmann F, Hielscher R and Schaeben H (2011) Grain detection from 2d and 3d EBSD data—specification of the MTEX algorithm. *Ultramicroscopy*, **111**(12), 1720–1733

Bennington KO (1963) Some crystal growth features of sea ice. *Journal of Glaciology*, **4**(36), 669–688

Dempsey D and Langhorne P (2012) Geometric properties of platelet ice crystals. *Cold. Reg. Sci. Technol.*, **78**, 1–13

Dempsey DE, 5 others (2010) Observation and modeling of platelet ice fabric in McMurdo Sound, Antarctica. *J. Geophys. Res.*, **115**(C1), C01007 (doi: 10.1029/2008jc005264)

Drewry D, Jordan S and Jankowski E (1982) Measured properties of the Antarctic Ice Sheet: surface configuration, ice thickness, volume and bedrock characteristics. *Ann. Glaciol.*, **3**, 83–91

Eicken H, Lange MA and Dieckmann GS (1991) Spatial variability of sea-ice properties in the northwestern weddell sea. *J. Geophys. Res.*, **96**(C6), 10603

Foldvik A and Kvinge T (1974) Conditional instability of sea water at the freezing point. *Deep Sea Research and Oceanographic Abstracts*, **21**(3), 169–174

Gough AJ, 5 others (2012a) Signatures of supercooling: McMurdo Sound platelet ice. *Journal of Glaciology*, **58**(207), 38–50

Gough AJ, Mahoney AR, Langhorne PJ, Williams MJM and Haskell TG (2012b) Sea ice salinity and structure: a winter time series of salinity and its distribution. *Journal of Geophysical Research: Oceans*, **117**(C3), C03008 (doi: 10.1029/2011jc007527)

Gow A, Ackley S, Weeks W and Govoni J (1982) Physical and structural characteristics of Antarctic sea ice. *Ann. Glaciol.*, **3**, 113–117

Hillig W (1959) Kinetics of solidification from nonmetallic liquids. In Kingery W, ed. *Kinetics of high-temperature processes*. MIT Press, Cambridge, MA, 127–135

Hughes KG, Langhorne PJ, Leonard GH and Stevens CL (2014) Extension of an ice shelf water plume model beneath sea ice with application in McMurdo Sound, Antarctica. *Journal of Geophysical Research: Oceans*, **119**(12), 8662–8687

Iliescu D, Baker I and Chang H (2004) Determining the orientations of ice crystals using electron backscatter patterns. *Microscopy Research and Technique*, **63**(4), 183–187

Jeffries MO, Weeks WF, Shaw R and Morris K (1993) Structural characteristics of congelation and platelet ice and their role in the development of Antarctic land-fast sea ice. *Journal of Glaciology*, **39**(132), 223–238

Kawamura T and Ono N (1980) Freezing phenomena at seawater surface opening in polar winter: Measurement of crystallographic orientation of newly grown sea ice. *Low Temperature Science A*, **39**, 175–180

Kolmogorov AN (1976) Geometric selection of crystals. *Doklady Akad Nauk Minerologia USSR*

Langhorne PJ (1983) Laboratory experiments on crystal orientation in NaCl ice. *Ann. Glaciol.*, **4**, 163–169

Langhorne P and Robinson W (1986) Alignment of crystals in sea ice due to fluid motion. *Cold. Reg. Sci. Technol.*, **12**(2), 197–214

Langhorne PJ, 12 others (2015) Observed platelet ice distributions in Antarctic sea ice: an index for ocean-ice shelf heat flux. *Geophys. Res. Lett.*, **42**(13), 5442–5451

Langway C (1958) *Ice Fabrics and the Universal Stage*. Technical report - U.S. Army Snow Ice and Permafrost Research Establishment Corps of Engineers, Department of Defense, Department of the Army, Corps of Engineers, Snow Ice and Permafrost Research Establishment

Lewis EL and Perkin RG (1986) Ice pumps and their rates. *J. Geophys. Res.*, **91**(C10), 11756

Matsuda M (1979) Determination of *a*-axis orientations of polycrystalline ice. *Journal of Glaciology*, **22**(86), 165–169

Matsuda M and Wakahama G (1978) Crystallographic structure of polycrystalline ice. *Journal of Glaciology*, **21**(85), 607–620

McFarlane V, Loewen M and Hicks F (2014) Laboratory measurements of the rise velocity of frazil ice particles. *Cold. Reg. Sci. Technol.*, **106–107**, 120–130

McFarlane V, Loewen M and Hicks F (2015) Measurements of the evolution of frazil ice particle size distributions. *Cold Regions Science and Technology*, **120**, 45–55

McFarlane V, Loewen M and Hicks F (2017) Measurements of the size distribution of frazil ice particles in three alberta rivers. *Cold Regions Science and Technology*, **142**, 100–117

Miyamoto A, 5 others (2005) Ice fabric evolution process understood from anisotropic distribution of *a*-axis orientation on the GRIP (Greenland) ice core. *Ann. Glaciol.*, **42**, 47–52

Miyamoto A, Weikusat I and Hondoh T (2011) Complete determination of ice crystal orientation using Laue X-ray diffraction method. *Journal of Glaciology*, **57**(201), 103–110

Morawiec A (1995) Misorientation-angle distribution of randomly oriented symmetric objects. *J. Appl. Crystallogr.*, **28**(3), 289–293

Obbard R, Baker I and Sieg K (2006) Using electron backscatter diffraction patterns to examine recrystallization in polar ice sheets. *Journal of Glaciology*, **52**(179), 546–557

Pauling L (1935) The structure and entropy of ice and of other crystals with some randomness of atomic arrangement. *Journal of the American Chemical Society*, **57**(12), 2680–2684

Petrich C & Eicken H (2017) Overview of sea ice growth and properties. In Thomas DN, ed. *Sea Ice*. John Wiley & Sons, Ltd, Hoboken, United States, 1–41 (doi: 10.1002/9781118778371.ch1)

Piazolo S, Montagnat M and Blackford JR (2008) Sub-structure characterization of experimentally and naturally deformed ice using cryo-EBSD. *Journal of Microscopy*, **230**(3), 509–519

Prior DJ (1999) Problems in determining the misorientation axes, for small angular misorientations, using electron backscatter diffraction in the SEM. *J. Microsc.*, **195**(3), 217–225

Prior DJ, 13 others (1999) The application of electron backscatter diffraction and orientation contrast imaging in the SEM to textural problems in rocks. *Am. Mineral.*, **84**(11–12), 1741–1759

Prior D, 15 others (2015) Making EBSD on water ice routine. *J. Microsc.*, **259**(3), 237–256

Randle V (1992) *Microtexture Determination and Its Applications (Book)*. Maney Pub, Leeds, United Kingdom, ISBN 9780901716354

Randle V and Engler O (2009) *Introduction to Texture Analysis*. Taylor & Francis Inc, Bosa Roca, United States, ISBN 1420063650

Smith IJ, 5 others (2001) Platelet ice and the land-fast sea ice of McMurdo Sound, Antarctica. *Ann. Glaciol.*, **33**(1), 21–27.

Treverrow A, Warner RC, Budd WF and Craven M (2010) Meteoric and marine ice crystal orientation fabrics from the Amery Ice Shelf, East Antarctica. *Journal of Glaciology*, **56**(199), 877–890

Tucker WB, Gow AJ and Richter JA (1984) On small-scale horizontal variations of salinity in first-year sea ice. *J. Geophys. Res.*, **89**(C4), 6505

Weeks W (2010) *On Sea Ice*. University of Alaska Press, Alaska, United States, ISBN 160223079X

Weeks WF and Gow AJ (1980) Crystal alignments in the fast ice of arctic alaska. *J. Geophys. Res.*, **85**(C2), 1137

Wheeler J, Prior D, Jiang Z, Spiess R and Trimby P (2001) The petrological significance of misorientations between grains. *Contributions to Mineralogy and Petrology*, **141**(1), 109–124

Wongpan P, Langhorne PJ, Dempsey DE, Hahn-Woernle L and Sun Z (2015) Simulation of the crystal growth of platelet sea ice with diffusive heat and mass transfer. *Ann. Glaciol.*, **56**(69), 127–136